Int. J. Electrochem. Sci., 17 **(2022)** Article Number: 220513, doi: 10.20964/2022.05.19

International Journal of
ELECTROCHEMICAL
SCIENCE
www.electrochemsci.org

Interface Modification of NASICON-structured $Li_{1.5}Al_{0.5}Ge_{1.5}(PO_4)_3$ (LAGP) by Femtosecond Laser Structuring and Ionic Liquid

Binggong Yan[1], Yongchao Wang[1], Hongliang Ren[2], Xizhao Lu[1], Masashi Kotobuki[3], Bin Liu[1], Kaiyong Jiang[1,]*

[1] Fujian Key Laboratory of Special Energy Manufacturing, Xiamen Key Laboratory of Digital Vision Measurement, Huaqiao University, Xiamen, China
[2] Fujian Key Laboratory of Light Propagation and Transformation, Huaqiao University, Xiamen, China
[3] Battery Research Center of Green Energy, Ming Chi University of Technology, New Taipei City, Taiwan
*E-mail: jiangkyhqu@163.com

Received: 9 December 2021 / *Accepted:* 3 February 2022 / *Published:* 5 April 2022

NASICON-structured solid-state electrolyte, namely $Li_{1.5}Al_{0.5}Ge_{1.5}(PO_4)_3$ (LAGP) possesses high ionic conductivity and good compatibility with lithium metal that make it an ideal electrolyte for next-generation lithium battery. However, high interfacial impedance and possible dendrite limit its practical applications. To reduce interfacial impedance, herein, surface texturing on the LAGP is conducted using a femtosecond laser, and further wetted by ionic liquids. The femtosecond laser-modified surface can effectively increase wettability and improve the interfacial contacts. Low area specific impedance of 81.4Ω cm^{-2} is obtained and the full battery demonstrates good electrochemical performances.

Keywords: solid state battery, femtosecond laser structuring, ionic liquid, interfacial engineering, surface texture

1. INTRODUCTION

Lithium-ion batteries (LIBs) with high energy density and long cycle life have been widely used in consumer devices such as cell phones, laptops and electric vehicles[1-5]. However, due to the toxicity, narrow electrochemical window, low thermal stability, leakage and flammability of organic liquid electrolytes, the conventional LIBs face many safety issues. To solve these issues, it is necessary to replace liquid electrolyte with solid electrolyte.

NASICON structured $Li_{1.5}Al_{0.5}Ge_{1.5}(PO_4)_3$ (LAGP) has attracted a lot of attentions in the past years owing to the advantages of wide electrochemical windows, high thermal stability and good

mechanical properties[6-10]. The major challenges for the large-scale practical use of LAGP are (1) the limited contact area, poor interfacial stability and high interfacial resistance between solid electrolyte and electrodes, (2) undesirable interfacial wettability between Li metal and LAGP preventing intimate physical contact, and (3) formation of Li dendrites owing to uneven deposition of Li metal and the inhomogeneous distribution of current at the electrode/electrolyte interface, which may penetrate the solid-state electrolyte and cause short-circuit [11-13].

Considering these challenges, significant efforts have been devoted to increasing the contact area between electrolyte and electrodes. In traditional LIBs, electrodes with three-dimensional pore structures were proposed to increase electrolyte accessibility and enhance Li-ion diffusion kinetics, thereby, improve the rate capability of electrode, such as Si and C anodes[14], and lithium cobalt oxide [15,16] and lithium manganese oxide cathode [15, 16]. Three-dimensional structures lead to an increase in power density and capacity retention rate of LIBs due to large electrochemically active surface areas and shortened Li-ion pathways[17-21]. The purpose of this work is to improve the electrochemical performances of all-solid-state batteries through the surface texturing of inorganic solid-state electrolyte using a femtosecond laser. The periodic micro-grid texture is used to induce the uniform distribution of current on the both sides of LAGP. The enhancement of cell performance by grid texture is investigated by controlling the spacing of the grids. Moreover, introducing the ionic liquids (ILs) on the surface of textured LAGP to form a composite electrolyte not only improves the surface wettability and interfacial stability of electrolyte/electrode, but also further maximizes the accessibility of contact area to facilitate Li-ion transport to reduce interface resistance.

2. EXPERIMENTAL

Fig.1 schematically shows the deliberated design of surface texture on LAGP for high electrochemical performance.

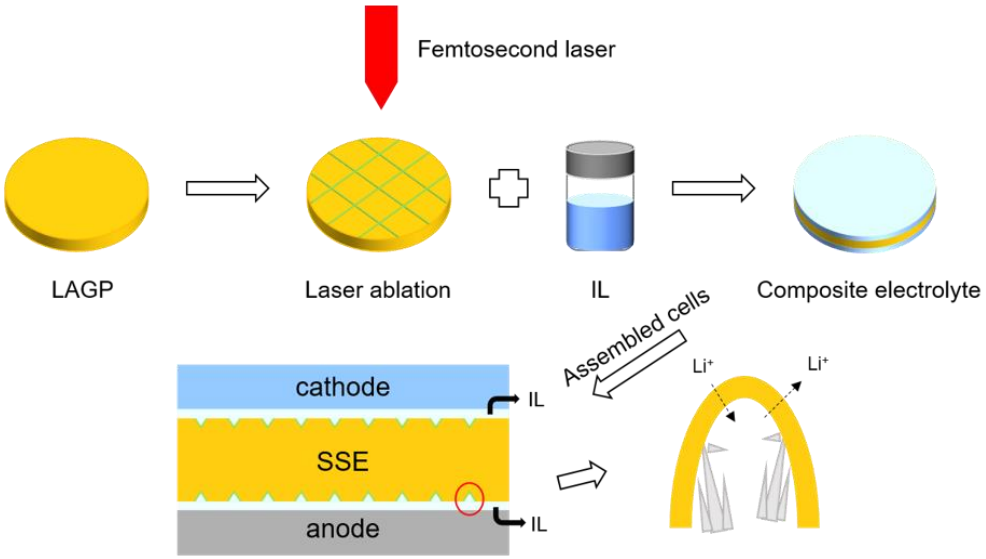

Figure 1. Schematic illustration of laser processing and assembled cells (IL stands for ionic liquid, SSE stands for Solid State Electrolyte)

The manufacturing process is categorized into three parts in which the micro-grid texture was structured by the femtosecond laser structuring process, after which, the non-flammable IL as a function of intermediate transition layer was added to the both sides of LAGP to enhance the contact quality between electrolyte and electrodes. And then, batteries were assembled by using lithium metal as the anode and $LiCoO_2$ as the cathode.

2.1 Materials preparation

The inorganic solid-state electrolyte LAGP was synthesized by conventional melt-quench process[19, 22]. The stoichiometric amount of lithium carbonate Li_2CO_3 (Aladdin, 99.99%), aluminum oxide Al_2O_3 (Aladdin, AR), germanium dioxide GeO_2 (Aladdin, 99.999%), and ammonium dihydrogen phosphate $(NH_4)H_2PO_4$ (SCR, AR) was weighted by the molar ratio of Li: Al: Ge: P=1.5: 0.5: 1.5: 3 with 10% excess Li to compensate Li loss in the preparing process. The precursors were mixed by a ball-milling machine (Retsch PM100) with 200 r/min for 2h. The ball-milled powder was ground in an agate mortar for 10 minutes and then heated to 380℃ for 6h to decompose ammonia, after which, the powder was ground for 10 min again followed by calcined in a Pt crucible at 1380℃ for 2h. The molten LAGP was poured into a mold with an inner diameter of 12 mm that was pre-heated to 400℃. The mold was cool to room temperature in the air to get a glass rod. The glass rod was crystallized by heating it to 900°C at a heating rate of 5°C/min and then remained at 900°C for 8h. The crystallized LAGP rod was then sliced into thin disks with a thickness of 500μm using a *Diamond Wire Saw* (STX-202A).

The IL was prepared through dissolving 0.2M fraction Bis (trifluoromethane) sulfonamide lithium salt in 0.8M fraction of 1-Ethyl-3-methylimidazolium bis (trifluoromethylsulfonyl) imide, then, 5wt% EC/PC and 5wt% VC was added and stirred for 3h. All the procedures were carried out in an argon-filled glove box (O_2, H_2O < 0.1 ppm).

2.2 Laser structuring process

The laser structuring processes were performed using a femtosecond laser PHAROS-10W (Light Conversion) at a wavelength of 1030 nm and a laser power range from 0 to 10 W. The pulse duration was set at 228 fps and the repetition rate was set as 100 kHz. Micro-grid textures with different grid spaces ranging from 20 μm to 100 μm were prepared. For ease of expression, no-textured sample is named as Bare LAGP, no-textured sample wetted by ionic liquid is named as LAGP@IL, LAGP with different grid spaces from 20 μm to 100 μm and wetted by ionic liquid is separately named as LAGP@IL-20, LAGP@IL-40, LAGP@IL-60, LAGP@IL-80 and LAGP@IL-100. All the laser structuring processes were carried out under ambient air and room temperature.

2.3 Characterization

The surface morphology and the cross-section of the samples were investigated by Scanning Electron Microscopy (JSM-IT500, Japan) equipped with an energy-dispersive spectroscopy (EDS).

Li/LAGP@IL/Li symmetric cells were assembled by sandwiching thin lithium metal plates, ionic liquid and LAGP pellets. AC-impedance measurements of the symmetric cells were conducted using an Electrochemical Workstation (IM6, Germany) in a frequency ranging from 1 MHz to 0.1 Hz. The data were analyzed and fitted by customized equivalent circuits using Z-View. The galvanostatic cycling of lithium symmetrical cells was performed at a current density of 0.05mA cm^{-2} and a capacity density of 0.05mAh cm^{-2}.

The electrochemical performances of the full batteries (Li/LAGP@IL-X/Li (X=grid space 20 μm, 40 μm, 60 μm, 80 μm, 100 μm)) were measured with a charge-discharge instrument (Neware, China). The cathode was prepared by mixing 80 wt% $LiCoO_2$ active material, 10 wt% polyvinylidene fluoride (PVDF) and 10 wt% carbon black dissolved in N-methyl2-pyrrolidene (NMP), the resulting slurry was pasted onto aluminum foil and dried at 80 ° C for 12 h.

3. RESULTS AND DISCUSSION

It is essential to optimize the parameters of the femtosecond laser structuring process to ensure the grain integrity during laser processing without influencing the transport of Li^+. In this work, the laser power (P), scanning speed (V) and laser processing times (N) were optimized.

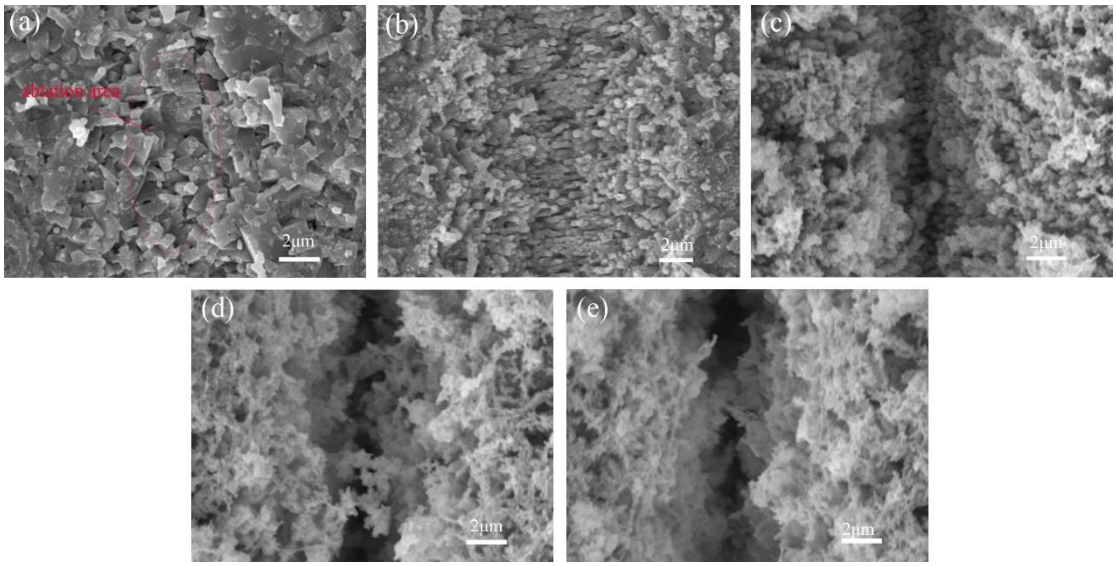

Figure 2. SEM images of LAGP after the femtosecond laser processing at V=1mm/s. (a) P=1.0W, (b) P=1.5W, (c) P=2W, (d) P=2.5W, (e) P=3W

Fig. 2 shows the change of the LAGP surface morphology with the increased laser power. When the laser power was 1 W (Fig. 2(a)), limited materials can be etched and the textured grooves cannot be identified clearly. When the laser power was increased to 1.5W (Fig. 2 (b)), the textured grooves were clearly observed, although the V-shaped grooves at the bottom were not completely vaporized due to the diffusing path of the plasma was blocked. With the increase of laser power, flocculent materials appeared

in the V-shaped grooves and tended to fill the grooves gradually. Therefore, 1.5 W was selected as the laser power for further experiments.

Fig. 3 reveals the morphologies of grooves at various scanning speeds. With the increase of scanning speed, the number of particles in the grooves gradually decreased, and a groove was clearly observed when the scanning speed was 20 mm/s (Fig.3 (e)). To obtain more contacting area between the electrodes and electrolyte, it is necessary to improve the depth to width ratio of the grooves, so, 20 mm/s was used as the scanning speed for further experiments.

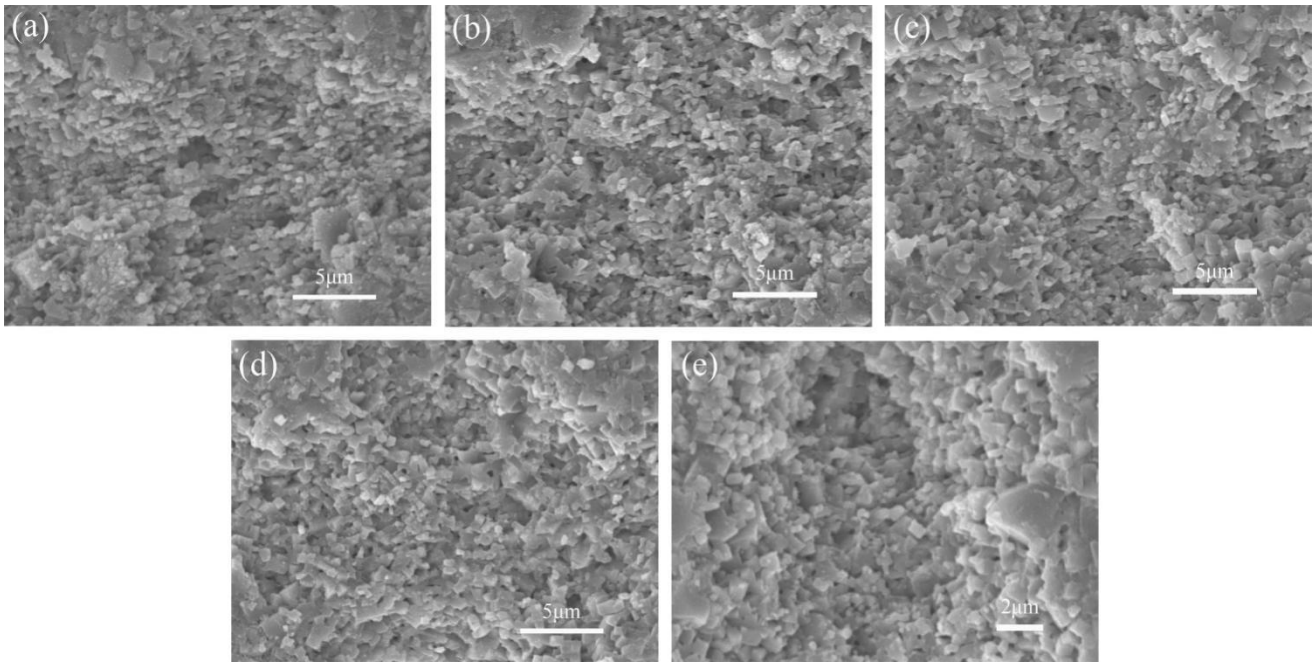

Figure 3. Effect of scan speed on morphology when P=1.5W. **(**a) V=1mm/s, (b) V=5mm/s, (c) V=10mm/s, (d) V=15mm/s, (e) V=20mm/s

Fig. 4 exhibits the influence of the number of scanning times on the morphology of LAGP when the laser power and scanning speed were fixed at 1.5W and 20mm/s respectively. As can be seen from Fig. 3, when N > 5, the grooves formed. Based on the above results, the optimized parameters of the femtosecond laser structuring process of LAGP including laser power, scanning speed and scanning times were determined to be 1.5 W, 20 mm/s and 5, respectively.

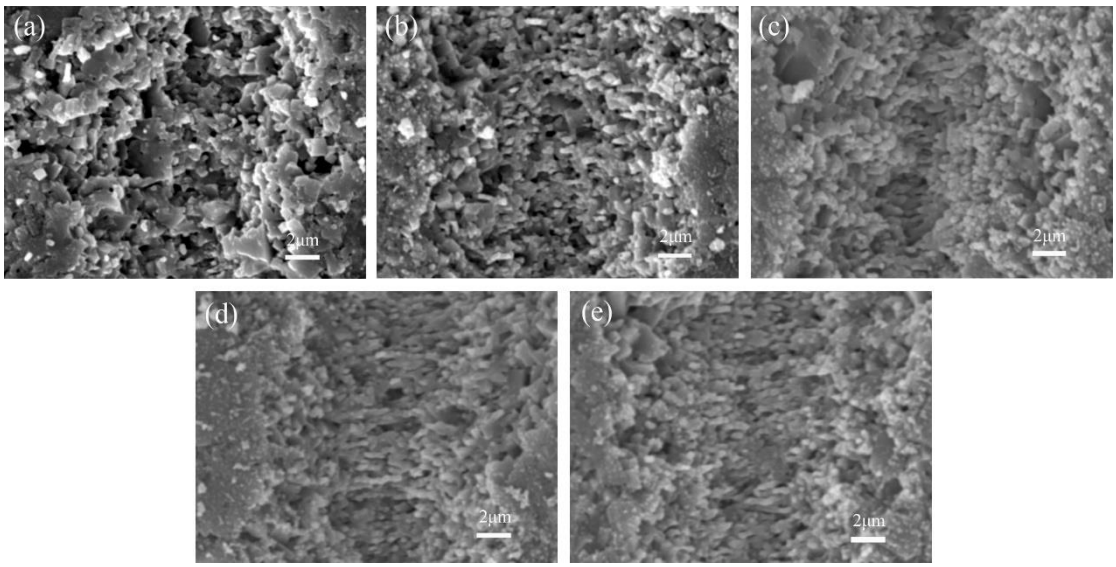

Figure 4. P=1.5W, V=20mm/s. (a) N=1, (b) N=5, (c) N=10, (d) N=15, (e) N=20

Fig. 5a, b shows the grid texture and corresponding cross-section of the LAGP that etched by the optimized femtosecond laser structuring process. As can be seen from Fig. 5a, regular grooves were successfully prepared on LAGP, and the depth of the grooves was about 15 μm that can be identified in Fig. 5b. X-ray diffraction (XRD) was used to analyze the influence of the laser structuring process on the crystal structure of LAGP (Fig.5c). The peaks of all the specimens matched well with the reported NASICON structure [23-25]. Low intensity GeO_2 diffraction peak appeared in the vicinity of 2θ=21°, indicating that laser structuring process induced a limited phase separation of GeO_2 from LAGP.

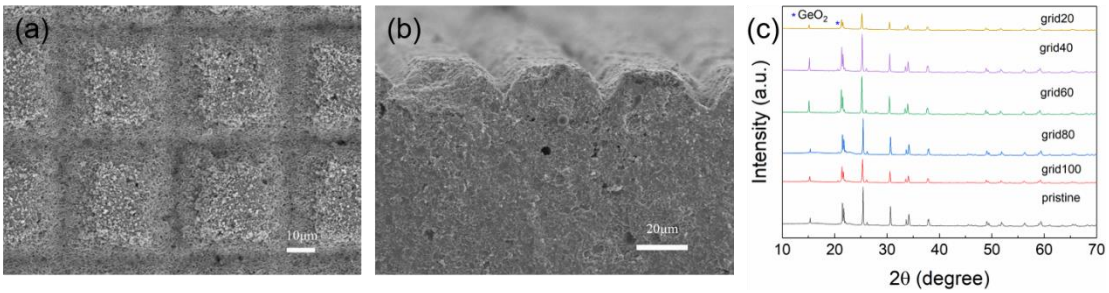

Figure 5. (a) The grid texture, (b) cross-sectional topography ablated by femtosecond laser, (c) XRD pattern of samples ablated by femtosecond laser

The contact angles (CA) between the IL and solid-state electrolyte LAGP with different grid spaces are presented in Fig. 6a. With the increase of grid space, the CA firstly decreased and then increased gradually. The minimum CA 18° was obtained when the grid spacing was 40 μm. Compared with the no-textured sample (CA=42°) (Fig. 6b), the grid texture can provide better surface wettability, increase the contact area between electrolyte and electrodes, and thus regulate the current density at the interface to retard Li stripping and amplify the mechanical stress near the interface to facilitate Li

creep[26].

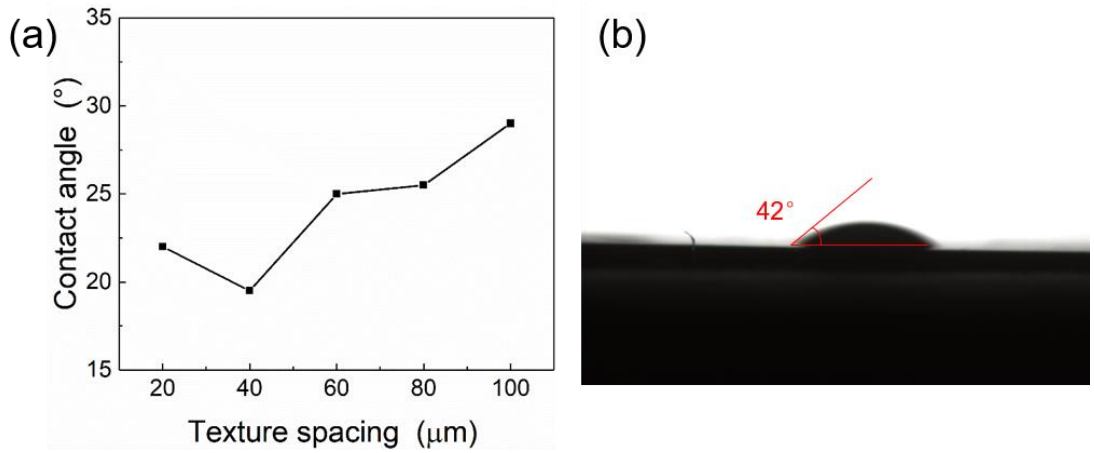

Figure 6. (a) The tendency of contact angle (CA) with different grid spacing, (b) the CA photograph of the no-textured sample

The Nyquist plots of AC impedance spectra of the symmetric cell in the format of Li/LAGP/Li and Li/LAGP@IL/Li are shown in Fig.7a. The impedance of the symmetric cell with the hybrid electrolyte was largely reduced comparing with the Li/LAGP/Li cell because the interface contact was changed from solid to solid point contact to liquid to solid contact. Fig.7b shows the impedance spectra of the hybrid electrolyte with different grid spaces. The total impedance of bare LAGP is about 75Ω as shown in Fig.7c that measured by Au/LAGP/Au. The impedance values of each specimen under Z-View fitting and the corresponding area specific resistance are listed in Table 1. The total resistances and the area specific resistances for most of the samples with micro-grid textures are lower than the no-textured samples. A minimum area specific resistance of 10 Ω/cm^2 was obtained when the grid space was 40 μm which is consistent with the CA results. This indicates that interfacial resistance can be reduced by femtosecond laser structuring on LAGP [20, 26].

In addition to decreasing the interfacial resistance, the micro-grid texture also positively impacts the electrochemical cycling behavior. A comparison of cycling performance of Li/LAGP/Li and $LiCoO_2$/LAGP@IL-X/Li is shown in Fig.7d. The potential of bare LAGP increases sharply at the beginning of the application of the current which due to the large area specific resistance, while the hybrid electrolyte shows relatively stable cyclic performances. The cyclic performances of the symmetrical cell with different grid spaces are shown in Fig.7e. The batteries with grid textures show a short failure time, which may result from the reduction of shear modulus of LAGP by laser structuring process. When the batteries were disassembled, uniformly distributed black area and white powder around LAGP can be found (Fig.7f), which is consistent with the results reported by Corr et al [27], indicated structural decomposition of LAGP at low voltage. The increase of overpotential of the batteries may result from the crystallization of ionic liquid and interface decomposition.

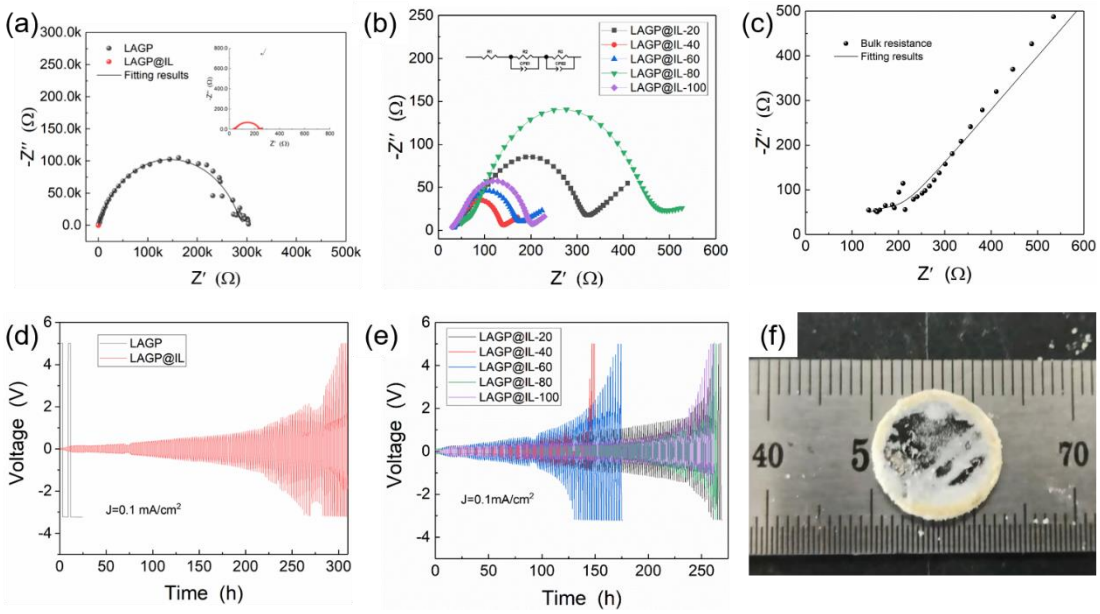

Figure 7. a) Impedance spectra measured at room temperature for bare LAGP and hybrid electrolyte, b) hybrid electrolyte with different grid spacing texture. Galvanostatic cycling of c) Li/LAGP/Li and d) Li/LAGP@IL/Li symmetrical cell with a current density of 0.1mA/cm^2 at room temperature. e) Galvanostatic cycling of Li/LAGP@IL-X/Li symmetrical cell. f) One side of LAGP after cycling.

Table 1. The impedance value of each semicircle under Z-View fitting and the corresponding specific area resistance of the samples.

Sample	Area specific resistance (Ω cm^{-2})
Bare LAGP	199878
LAGP@IL	88
LAGP@IL-20	132
LAGP@IL-40	10
LAGP@IL-60	35
LAGP@IL-80	185
LAGP@IL-100	60

$LiCoO_2$/LAGP@IL-X/Li cells were assembled to evaluate the electrochemical performances of the hybrid electrolyte. Fig.8a shows the charge-discharge curves of the cells with different micro-grid textures for the first cycle in the voltage range of 3.0-4.55 V at a current of 20 μA at room temperature. It can be seen from Fig. 8a that the specimens etched by femtosecond laser show higher charge-discharge capacity. When the grid space is 80 μm, the maximum charge-discharge capacity achieved at 105 and 87 mAh g^{-1}, respectively, with a coulombic efficiency of ~78%. While the charge-discharge capacity of the no-textured sample is ~87 and ~37 mAh g^{-1}, respectively, with a coulombic efficiency of ~42%. Fig.8b shows the cycle performance of the $LiCoO_2$/LAGP@IL-X/Li cells with different micro-grid textures at a rate of 0.1C. Comparing with the no-textured sample, the cells with different micro-grid textures show higher discharge capacity and capacity retention. The higher the texture coverage, the higher the

discharge capacity. Fig.8c shows the cross-sectional SEM image of the grid texture after cycling. The surface of the groove was covered with tiny particles, while the corresponding graph of elemental distribution showed weak P and Ge signals (Fig.8d, e). This indicated that the particles are not phosphate or germanium derivatives. The improve of the capacity should be attributed to the enhancement of the diffusion channels of lithium ions by the micro-grid textures [28, 29].

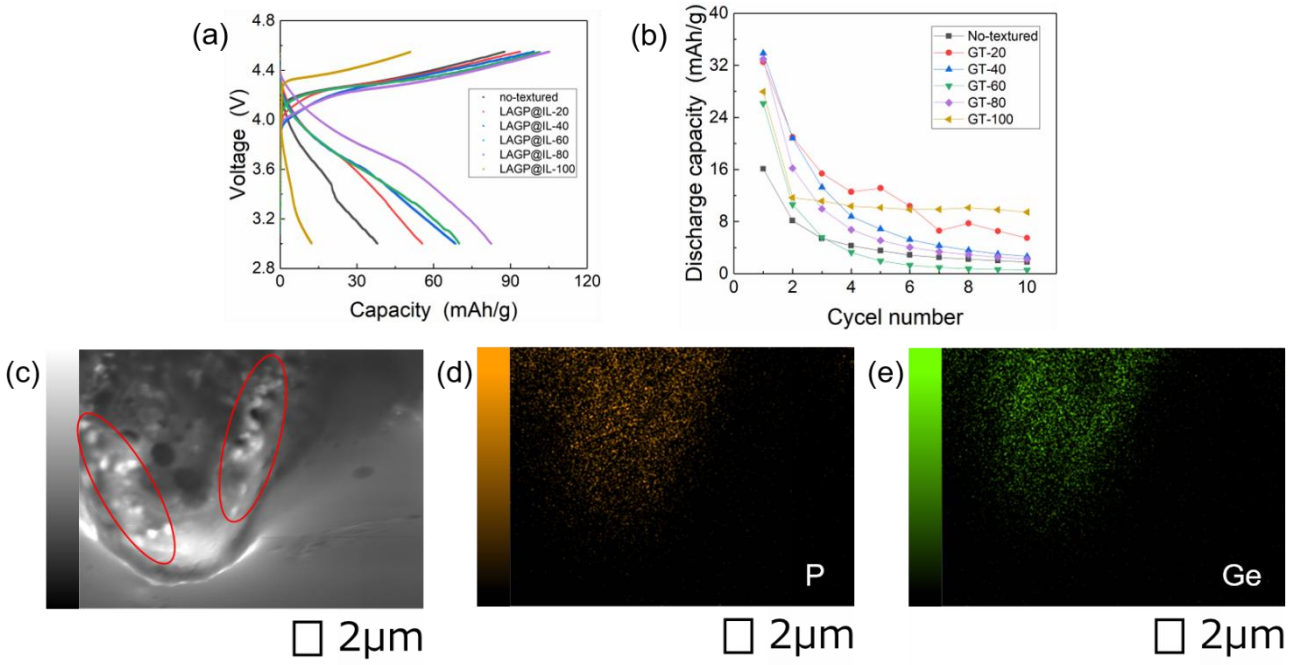

Figure 8. (a) Charge-discharge curves of the LCO/LAGP@IL-X/Li (X=grid spacing) cell at a current density of at current of 20μA at room temperature. (b) Rate performance of $LiCoO_2$/LAGP@IL-X/Li cell at rates of 0.1C. (c) Cross-section of the grid texture and the corresponding graph of elemental distribution for (d) P and (e) Ge.

4. CONCLUSIONS

We demonstrated a method of interfacial engineering for solid-state electrolyte LAGP based on femtosecond laser processing. Good surface morphology and grain integrity were obtained by optimizing laser parameters. Composite electrolyte was prepared by introducing ionic liquid to LAGP. The laser-ablated LAGP with grid textures and IL exhibits good interfacial wettability. The interfacial resistance of the LAGP with grid textures is much smaller than the no-textured samples, and a low area specific resistance of 81.4 Ω cm^{-2} was achieved when the grid spacing is 40 μm. Related solid-state batteries showed good charge-discharge capacity and capacity retention. Interfacial engineering by femtosecond laser processing provides a new strategy for improving the interfacial performances of all solid-state batteries.

ACKNOWLEDGMENT
This work was supported by the Engineering Research Center of Digital Graphic and Next-generation Printing in Jiangsu Province (SDGC2136), Open Project Program of Fujian Key Laboratory of Light Propagation and Transformation (KF2021104) and Subsidized Project for Postgraduates' Innovative Fund in Scientific Research of Huaqiao University.

References

1. P. He, H. Yu, D. Li, H. Zhou, *J. Mater. Chem*., 22 (2012) 368.
2. A. Manthiram, X. Yu, S. Wang, *Nat. Rev. Mater*., 2 (2017).
3. J. B. Goodenough, K. Park, *J. Am. Chem. Soc*., 135 (2013) 1167.
4. J. M. Tarascon, M. Armand, *Nature*, 414 (2001) 359.
5. B. Scrosati, J. Garche, *J. Power Sources*, 195 (2010) 2419.
6. S. Song, H. M. Duong, A. M. Korsunsky, N. Hu, L. Lu, *Sci. Rep.-Uk*, 6 (2016).
7. F. Zheng, M. Kotobuki, S. Song, M. O. Lai, L. Lu, *J. Power Sources*, 389 (2018) 198.
8. Y. Liu, C. Li, B. Li, H. Song, Z. Cheng, M. Chen, P. He, H. Zhou, *Adv. Energy Mater*., 8 (2018) 1702374.
9. C. R. Mariappan, C. Yada, F. Rosciano, B. Roling, *J. Power Sources*, 196 (2011) 6456.
10. X. Xu, Z. Wen, X. Wu, X. Yang, Z. Gu, *J. Am. Ceram. Soc*., 90 (2007) 2802.
11. X. Cheng, R. Zhang, C. Zhao, Q. Zhang, *Chem. Rev*., 117 (2017) 10403.
12. P. Verma, P. Maire, P. Novák, *Electrochim. Acta,* 55 (2010) 6332.
13. A. Sakuda, A. Hayashi, M. Tatsumisago, *Chem. Mater*., 22 (2010) 949.
14. J. S. Kim, W. Pfleging, R. Kohler, H. J. Seifert, T. Y. Kim, D. Byun, H. Jung, W. Choi, J. K. Lee, *J. Power Sources,* 279 (2015) 13.
15. D. G. Lim, D. Chung, R. Kohler, J. Proell, C. Scherr, W. Pfleging, R. E. García, *J. Electrochem. Soc.*, 161 (2013) A302.
16. R. Kohler, J. Proell, M. Bruns, S. Ulrich, H. J. Seifert, W. Pfleging, *Appl. Phys*. A, 112 (2013) 77.
17. J. Pröll, R. Kohler, M. Torge, S. Ulrich, C. Ziebert, M. Bruns, H. J. Seifert, W. Pfleging, *Appl. Surf. Sci.*, 257 (2011) 9968.
18. J. Pröll, H. Kim, A. Piqué, H. J. Seifert, W. Pfleging, *J. Power Sources*, 255 (2014) 116.
19. B. Yan, L. Kang, M. Kotobuki, L. He, B. Liu, K. Jiang, *J. Solid State Electrochem*., 25 (2021) 527.
20. J. Wan, J. Xie, X. Kong, Z. Liu, Y. Cui, *Nat. Nanotechnol*., 14 (2019) 705
21. C. Zhao, Q. Sun, J. Luo, J. Liang, X. Sun, *Chem. Mater*., 32 (2020) 10113.
22. B. Yan, L. Kang, M. Kotobuki, F. Wang, K. Jiang, *Mater. Tech*., 34 (2018) 1.
23. Y.C. Kim, K.N. Jung, J.W. Lee, M.S. Park, *Ceram. Int*., 46 (2020) 23200.
24. J. Gao, J**.** Wu**,** S**.** Han**,** J**.** Zhang**,** W**.** Tang, *Funct. Mater. Lett*., 14 (2021) 2140001.
25. M. Abramchuk, A.A. Voskanyan, Y. Arinicheva, K. Lilova, A. Navrotsky, *J. Phys. Chem. Lett*., 12 (2021) 4400.
26. R. Xu, F. Liu, Y. Ye, H. Chen, R. Yang, Y. Ma, W. Huang, J. Wan, Y. Cui, *Adv. Mater*., 33 (2021) 2104009.
27. I. Mcclelland, S.G. Booth, H. El-Shinawi, B. Johnston, S.A. Corr, *ACS Appl. Energy Mater*., 4 (2021) 1527.
28. Z.Tai, Y. Liu, Z. Yu, Z. Lu, O. Bondarchuk, Z. Peng, L. Liu, *Nano Energy*, 94 (2022) 106947.
29. M.R. Busche, T. Leichtweiss, C. Fiedler, T. Drossel, J. Janek, *Adv. Mater. Interfaces*, 7 (2020) 2000380.